Computer Methods in Biomechanics and Biomedical Engineering, 2015
Vol. 18, No. 9, 981–992, http://dx.doi.org/10.1080/10255842.2013.865024

Taylor & Francis
Taylor & Francis Group

Experimental and computational investigation of the patient-specific abdominal aortic aneurysm pressure field

R. Antón[a]*, C.-Y. Chen[b], M.-Y. Hung[b], E.A. Finol[c] and K. Pekkan[b]

[a]*Department of Mechanical Engineering, Tecnun-University of Navarra, Paseo de Manuel Lardizábal 13, San Sebastián, Gipuzkoa 20018, Spain;* [b]*Department of Biomedical Engineering, Carnegie Mellon University, Pittsburgh, PA 15213, USA;* [c]*Department of Biomedical Engineering, The University of Texas at San Antonio, San Antonio, TX 78249, USA*

(*Received 30 March 2012; accepted 8 November 2013*)

The objective of the present manuscript is three-fold: (i) to study the detailed pressure field inside a patient-specific abdominal aortic aneurysm (AAA) model experimentally and numerically and discuss its clinical relevance, (ii) to validate a number of possible numerical model options and their ability to predict the experimental pressure field and (iii) to compare the spatial pressure drop in the AAA before and after the formation of intraluminal thrombus (ILT) for a late disease development timeline. A finite volume method was used to solve the governing equations of fluid flow to simulate the flow dynamics in a numerical model of the AAA. Following our patient-specific anatomical rapid prototyping technique, physical models of the aneurysm were created with seven ports for pressure measurement along the blood flow path. A flow loop operating with a blood analogue fluid was used to replicate the patient-specific flow conditions, acquired with phase-contrast magnetic resonance imaging, and measure pressure in the flow model. The Navier–Stokes equations and two turbulent models were implemented numerically to compare the pressure estimations with experimental measurements. The relative pressure difference from experiments obtained with the best performing model (unsteady laminar simulation) was ~1.1% for the AAA model without ILT and ~15.4% for the AAA model with ILT (using Reynolds Stress Model). Future investigations should include validation of the 3D velocity field and wall shear stresses within the AAA sac predicted by the three numerical models.

Keywords: computational fluid dynamics; aneurysm; pressure gradient; pressure tap; rapid prototyping

1. Introduction

Abdominal aortic aneurysms (AAAs) are found in 8.8% of the human population above 65 years of age (Newman et al. 2001). They cause about 15,000 deaths per year only in USA (Sakalihasan et al. 2005), and 1.3% of all deaths among men aged 65–85 years in developed countries (Thompson 2003). The pathogenesis and exact cause of formation of intraluminal thrombus (ILT) inside the AAA sac are not clear. It has been hypothesised that ILT formation is a multifactorial process, with both biological and mechanical factors playing a role and closely coupled to aneurysm expansion. Early AAA patient-specific studies ignored the thrombus entirely and flow simulations that incorporated a thrombus model are scarce (see, e.g. Bluestein et al. 2009). From a clinical and rupture risk assessment perspective, the growth rate of the aneurysm and ILT are critical. Therefore, a comparison of haemodynamic conditions in the AAA sac with and without thrombus is a worthwhile task because continuous patient-specific data on ILT and AAA growth is difficult to obtain given the asymptomatic nature of the disease.

A significant research effort has been devoted to study different aspects of AAA biomechanics extensively (Bluestein et al. 1996; Salsac et al. 2006; Biasetti et al. 2010), including geometry quantification and numerical modelling of flow and structure by our laboratory (Finol and Amon 2002; Scotti et al. 2005, 2008; Scotti and Finol 2007; Rodriguez et al. 2009; Shum et al. 2010; Shum, Martufi et al. 2011; Shum, Xu et al. 2011). In spite of this research work, few experimental studies performed measurements of the spatial pressure drop inside the AAA model. The limited information on AAA pressure drop is either utilised through non-patient-specific models or by exclusion of the iliac arteries, i.e. using only one inlet and one outlet. Peattie et al. (2004) reported pressure drop along an AAA model but without the iliac bifurcation; similar work was carried out by Dorfmann et al. (2010). Both studies concluded that there is little pressure variation along the AAA. Swillens et al. (2008) studied the effect of an AAA on wave reflection in the aorta. They also measured the pressure-time histories in a model with the iliac bifurcation (for models before and after AAA repair). However, in that case, the focus was not on the difference of the pressure variation due to the presence of the ILT and the difference in the pressure variation for an AAA model before and after repair was not very large. AAA rupture occurs when intraluminal pressure reaches a threshold that causes wall stress to exceed the yield stress

*Corresponding author. Email: ranton@tecnun.es

of the diseased tissue. The factors involved in the onset and growth of AAA are not known due to the asymptomatic nature of the disease. However, AAA rupture is a mechanical event, and therefore, variables like anisotropy of the wall constitutive material, the non-uniform distribution of wall thickness, the absolute pressure and the continuous cyclic pressure gradient at certain locations are hypothesised to relate to rupture risk. This work is focused on the analysis of the pressure gradient (i.e. independent of the absolute pressure) at peak systole, which is of the same order of magnitude of the maximum cyclic pressure gradient, and its location in the AAA sac.

In the present effort, we have used a patient-specific AAA geometry with and without ILT to investigate the pressure field in the AAA sac both numerically and experimentally. Both models include the common iliac arteries because entry into these arteries is an area prone to have high pressure gradients. The boundary conditions are derived from a phase-contrast magnetic resonance imaging (PC-MRI) exam taken by the subject at Allegheny General Hospital (Pittsburgh, PA, USA) following an Institutional Review Board (IRB) approved protocol. Several modelling alternatives are investigated in relation to the experimental measurements for the validation of the pressures predicted computationally.

2. Methods

2.1 *Image segmentation and 3D reconstruction*

The AAA geometry for the numerical and experimental models was obtained following acquisition of the subject's contrast-enhanced computed tomography (CT) images at the last follow-up exam prior to elective aneurysm repair at Allegheny General Hospital. The medical images were segmented following a level set algorithm and the three-dimensional (3D) reconstruction was performed using Simpleware (Simpleware Ltd, Exeter, UK). Surface irregularities resulting from the reconstruction process were subsequently removed using a low-pass filter based algorithm and a surface mesh representing the AAA lumen (with and without ILT) was generated for further manipulation of the geometry. The 3D surface underwent further removal of imperfections resulting from the image segmentation process using smoothing algorithms in Geomagic (Geomagic, Inc., Morrisville, NC, USA). The resulting AAA geometries are illustrated in Figure 1.

2.2 *Numerical model –mesh generation*

For Computational Fluid Dynamics (CFD) simulations that employ turbulence models, a high quality mesh is important to achieve numerical convergence with a reasonable computational cost. The Gambit 2.4 (2010; Ansys, Inc., Canonsburg, PA, USA) grid generation package was used to generate the AAA meshes. Assessment of the mesh quality was defined as devoid of high cell skewness as there is a known relationship between mesh quality, simulation convergence and convergence time (Antiga et al. 2002).

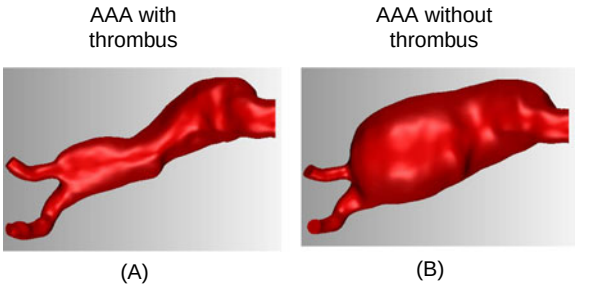

Figure 1. Geometry of the patient-specific AAA with (A) and without ILT (B).

Three types of meshes were generated to decide on an optimal meshing strategy: Type A mesh is generated from tetrahedral elements spaced with increasing densities using the size functions close to the walls. Type B mesh was constructed by first dividing the model into several subdomains. Combinations of hexahedral and tetrahedral elements are used in these domains (always using a finer mesh close to the wall). Finally, Type C mesh was a hybrid mesh in which the core of the whole volume was hexahedral elements, and for the finer mesh close to the wall, tetrahedral elements were used. To resolve the boundary layer close to the walls, size functions were used in Gambit, which allow the mesh topology to be controlled in the proximity of the entities to which they are attached. In the present case, the size of the wall cells is defined together with a mesh growth factor and a maximum cell size. The three types of mesh are illustrated in Figure 2. Primarily based on the use of cell skewness quality parameter, it was found that Type A provided the best mesh quality and employed in this work.

A mesh density sensitivity analysis was performed for the selected mesh strategy and for both models. The mesh density refinement was done using several size functions; the parameters of these size functions and the number of elements appears in Table 1.

The chosen mesh was Mesh 1. This has 0.85 million cells for the model with ILT and 1.4 million cells for the model without ILT. This mesh was obtained using size functions having additional details for the cells: length start size, 0.5 mm; growth factor for adjacent cell layers, 1.5 and maximum length size, 2.5 mm. The relative difference between Mesh 1 and Mesh 2 is $<0.8\%$ (for both models: with and without ILT) of the pressure drop between the inlet and the two outlets. That same relative difference for Mesh 2 and Mesh 3 is $<0.35\%$ (for both models: with and without ILT).

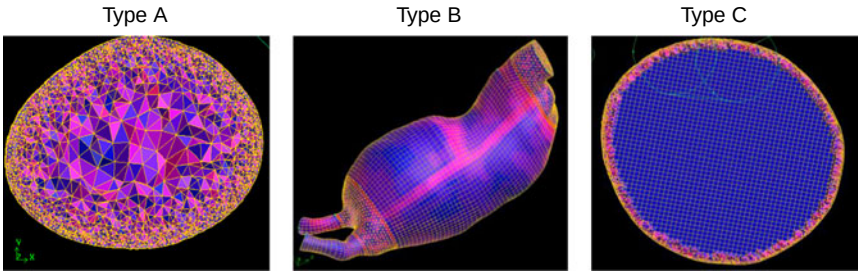

Figure 2. Types of meshes analysed in this study: Type A (one domain with tetrahedral elements), Type B (subdomains based on either hexahedral elements or tetrahedral elements) and Type C (one hybrid domain using hexahedral and tetrahedral elements).

Table 1. Parameters of the size functions (in mm) used to generate three meshes.

AAA without ILT	Mesh 1	Mesh 2	Mesh 3	AAA with ILT	Mesh 1	Mesh 2	Mesh 3
Start size	0.5	0.4	0.3	Start size	0.5	0.4	0.3
Growth rate	1.5	1.4	1.4	Growth rate	1.5	1.4	1.3
Max. size	2.5	2	2	Max. size	2.5	2	2
Number of elements	1.4 M	2.3 M	3.73 M	Number of elements	0.85 M	1.5 M	2.95 M

2.3 Numerical model – mathematical modelling and turbulence models

Both laminar (steady and unsteady approaching) and commonly employed turbulent models were analysed in this study. The performance of two classes of turbulence models, the Realizable $k-\varepsilon$ model and the Reynolds Stress Model (RSM) and their more recent extensions are investigated.

Large artery AAA flow is governed by the 3D, unsteady, incompressible laminar and turbulent flow regimes. For the laminar prediction (including the unsteady term), the standard Navier–Stokes Equations (see Equation (1)) are used. In this and subsequent equations, tensor notation is employed and the nomenclature that is used is the following: u stands for the instantaneous velocity, υ is the kinematic viscosity and $\bar{p}$ is the instantaneous modified kinematic pressure (i.e. p/ρ where ρ is the density):

$$\frac{\partial u_i}{\partial t}+\frac{\partial(u_j u_i)}{\partial x_j}=-\frac{\partial \bar{p}}{\partial x_i}+\upsilon\frac{\partial^2 u_i}{\partial x_j^2}. \quad (1)$$

For the turbulent models, the Reynolds decomposed, time-average Navier–Stokes equations are used, per Equations (2) and (3). The Reynolds decomposition and its nomenclature are as follows: $u = U + u'$ and $p = P + p'$ (where u and p stands for the instantaneous velocity and pressure, U and P are the time average velocity and pressure and u' and p' are the fluctuating velocity and pressure, respectively).

$$\frac{\partial U_i}{\partial x_i}=0, \quad (2)$$

$$\frac{\partial U_i}{\partial t}+\frac{\partial(U_j U_i)}{\partial x_j}=-\frac{\partial \bar{P}}{\partial x_i}+\upsilon\nabla^2 U_i+\frac{\partial}{\partial x_j}\left(-\overline{u_i' u_j'}\right), \quad (3)$$

where $\bar{P}$ is the modified kinematic pressure and the unknowns $\overline{u_i' u_j'}$ constitute the second-moment statistical correlation or so-called Reynolds stresses. These unknown stress components are modelled in order to close the system of equations. The most popular model to approximate these terms is the eddy-viscosity turbulence model. The eddy-viscosity model is based on the Boussinesq assumption that makes an analogy between turbulent stresses and viscous stresses. Therefore, the Reynolds stresses are proportionally related to the velocity gradients by an eddy viscosity for turbulence. $\overline{u_i' u_j'} = -2\upsilon_t S_{ij} + 2/3\delta_{ij}k$, where ν_t is the eddy viscosity, k is turbulent kinetic energy and $S_{ij} = 0.5(\partial U_i/\partial x_j + \partial U_j/\partial x_i)$.

By dimensional analyses, the kinematic eddy viscosity can be expressed as the product of a turbulent length and velocity scale. The platform of transport equations may be closed by two additional transport equations of two parameters related with a turbulent length and velocity scale. This model implies that the length and velocity scales of the mean flow and of the turbulence are proportional and can be related by means of dimensional reasoning to turbulent kinetic energy, k, and one length-scale-related parameter like its dissipation rate, ε, $u = k^{0.5}$, $l = k^{1.5}\varepsilon^{-1}$. Considering the above assumption, the turbulent eddy viscosity can be derived as $\upsilon_t = C_\mu k^2 \varepsilon^{-1}$ (C_μ is a constant, see Launder and Spalding 1974), and it is valid only when local isotropy in the turbulence field is assumed. ε is given by Equation (4):

$$\varepsilon = v\overline{\frac{\partial u_i'}{\partial x_j}\frac{\partial u_i'}{\partial x_j}}. \quad (4)$$

Thus the two-equation eddy-viscosity model requires two additional transport equations for k and ε to solve the spatial and temporal variation of the local velocity scale and the length scale. Equation (5) represents the transport equation for the turbulent kinetic energy (σ_k is a constant, see Launder and Spalding 1974).

$$\frac{\partial k}{\partial t} + \frac{\partial (U_j k)}{\partial x_j} = \frac{\partial}{\partial x_j}\left[\left(v + \frac{v_t}{\sigma_k}\right)\frac{\partial k}{\partial x_j}\right] + v_t S^2 - \varepsilon. \quad (5)$$

In the Realizable k–ε model (see Shih et al. 1995), numerical clipping is introduced in the solver to remove unphysical values of variables, e.g. negative normal stresses. To achieve the realisability effect, the C_μ is no longer constant but a function of the turbulence fields, mean strain and rotation rates. As this model includes the effects of mean rotation in the definition of the turbulent viscosity, it usually performs better than the standard k–ε model for flows with streamline curvature.

In the case of the turbulent models, the enhanced wall (EW) function is used as these models cannot be integrated near the wall, and therefore, they require a wall function. The EW subdivides the near wall region into a viscous sublayer and a fully turbulent flow layer. In the viscous sublayer region, a one-equation turbulence model is used (where only the equation κ is solved) and ε is computed algebraically (Wolfshtein 1969). However, in the fully turbulent flow, the two-equation models are used, and thus, ε is computed from a transport equation.

The RSM is a second-moment closure turbulent model. This implies that there is a transport equation for each of the six Reynolds stresses, and therefore, it avoids the isotropic eddy viscosity assumption. There is also a need to model the dissipation of the Reynolds stresses, and this is done using a transport equation for the dissipation of the turbulent kinetic energy (see details in Launder et al. 1975).

2.4 Numerical model – solver details and flow conditions

The governing equations were solved with a second order segregated scheme using the solver Fluent 12.1 (2010; Ansys, Inc.). The pressure-velocity-coupling algorithm SIMPLE was used to solve the continuity equation. Under-relaxation factors have been used for pressure, momentum, turbulent kinetic energy and the dissipation rate of turbulence kinetic energy: 0.3, 0.7, 0.8 and 0.8, respectively. For the unsteady simulations, a second order implicit scheme was used. An absolute residual within the range 1×10^{-5}–5×10^{-7} is achieved in all the simulations reported in this manuscript.

The inflow boundary condition was a velocity profile corresponding to a flow rate of 110 cm^3/s, which is derived from the subject's phase velocity encoding MRI exam at peak systole. The flow split ratios which were measured in the flow bench were used as boundary conditions at the outlet boundaries of the common iliac arteries. These split ratios were 50:50 for the AAA model without ILT and 48:52 for the AAA model with ILT. The Reynolds number (Re) was 2233 for both AAA models. The onset of turbulence in a smooth, circular pipe occurs at approximately 2000–2300; in a complex geometry as an AAA, it is not known which is the critical Re. O'Rourke and McCullough (2010) measured the turbulence intensity with Laser Doppler Velocimetry under constant flow rate conditions inside a patient-specific AAA model, finding that in some cases, turbulence may appear at Re as small as 488. Furthermore, they measured turbulence intensity levels as high as 80–100% for $Re = 1860$. Because the onset of turbulence in complex geometries is case dependent, it is convenient to analyse the flow under both laminar and turbulent regimes.

2.5 Experimental set-up and methodology

The test rig consisted of a steady pump, tubing, flow meters and the AAA flow phantom. A frame to support the flow loop was assembled using aluminium slotted columns; the configuration is shown in Figure 3.

The AAA phantom was manufactured using rapid prototyping, yielding a rigid wall model. Because AAAs become stiffer with disease progression (Di Martino et al. 2001), it is reasonable to consider the wall as rigid from the

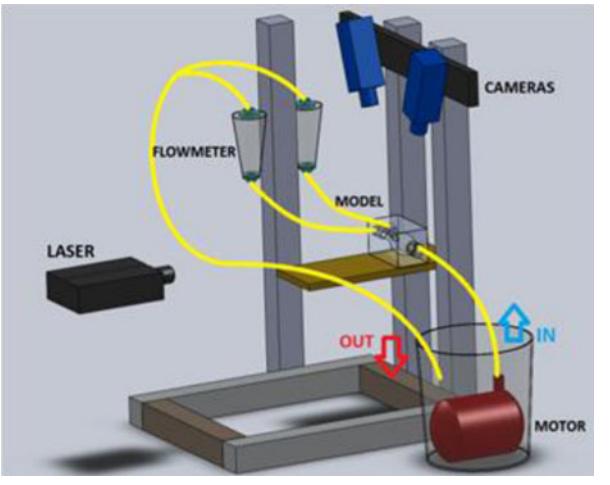

Figure 3. Schematic of flow loop set-up for the experimental AAA study. This flowbench is also used in Chen et al. (2014) for flow pattern visualization in an AAA using Stereoscopic Particle Image Velocimetry.

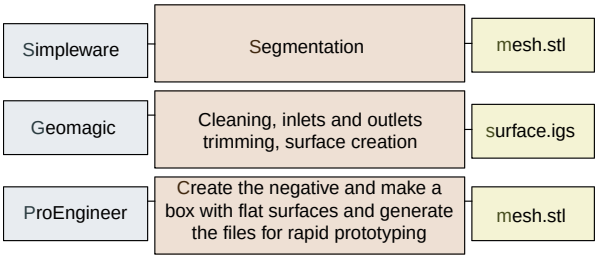

Figure 4. Strategy to obtain the numerical and physical models.

point of view of pressure gradient estimation. The rapid prototyping model was based on the negative of a 3D patient-specific model that was obtained from CT image reconstruction. The model sent to the rapid prototyping machine was built using Pro-Engineer (PTC, Parametric Technology Corporation, Needham, MA, USA). This process is summarised in Figure 4.

Once the rapid prototyping model was built, we drilled holes (2 mm diameter) to place the pressure taps (see Figure 5). The inlet was extended by more than 25 hydraulic diameters using a rigid tube and the outlets were extended by 6–8 hydraulic diameters.

The model includes the common iliac arteries because it has been observed numerically that including them is critical for accurate pressure, flow pattern and wall stress predictions (Frauenfelder et al. 2006). The flow rate used in the experiments (110 cm^3/s) was corresponding to the peak systolic flow of the cardiac cycle obtained from PC-MRI. The pressure gradient from the AAA sac to the iliac arteries is an adequate approximation of the maximum cyclic pressure gradient that would be obtained under pulsatile flow conditions.

The blood analogue fluid with a mixture of 34% glycerol and 46% water, resulting a density of 1.08 g/cm^3 and the viscosity of 3.5 cP (0.035 kg/m s) is utilised. Simultaneous measurements were performed using

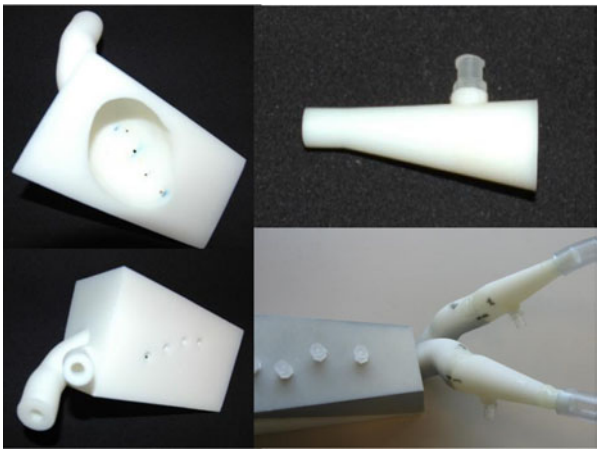

Figure 5. Details of the *in-vitro* AAA model and location of the pressure taps.

TruWave disposable pressure transducers (Edwards Life Sciences, Irvine, CA, USA) attached to a differential amplifier (WPI, Inc., Sarasota, FL, USA) in full bridge configuration (see Figure 6). Figure 6 also shows the location of pressure taps in both models, labelled as 1–7 from inlet to outlets.

The experimental protocol was as follows. First, the flow meters were calibrated with the blood analogue solution. Then, each of the pressure transducers was also calibrated and measurements were taken. Because the pressure taps were located at different heights, the procedure was to first open them to the atmosphere and measure the gauge pressure, and then, fill the flow loop with the blood analogue solution and measure the hydrostatic pressure at each of the pressure taps. Next, we ran the pump, waited a few seconds for a steady flow and then measured the static pressure at each of the locations (5000–6000 samples). Finally, the taps were opened again to the atmosphere and the gauge pressure was measured in case a small correction was needed (due to changes in the atmospheric pressure or small variations in the sensor). The repeatability was checked, using different pressure transducers for a given pressure tap and actual measurements were taken four times at the inlet and outlets and only twice at the pressure taps in the aneurysm sac (because pressure changes in the sac are relatively small compared to the neck and iliac arteries).

3. Results and discussion

3.1 CFD predictions and experimental validation

Four CFD mathematical models have been employed and the computed pressure fields for each model are analysed and compared with the corresponding experimental pressure drop measurements. The four CFD simulations are the following: first, a steady simulation using the Realizable $k-\varepsilon$ model; second, an unsteady simulation (with steady boundary conditions) also using the Realizable $k-\varepsilon$ model; third, an unsteady laminar simulation (with steady boundary conditions) and fourth, a steady simulation with the RSM model. In a simulation with constant boundary conditions as in the present work, both steady and unsteady simulations can be performed; both simulations will yield the same solution if there are no unsteady flow structures present. An example of unsteady structures is the vortex shedding (i.e. the Von Karman street) that takes place in (constant) flow across a cylinder. Because the AAA is a complex geometry, it is imperative not to disregard the unsteady nature of the numerical simulations.

3.1.1 AAA with ILT

Figure 7 presents the predicted pressure distribution in the aneurysm model with thrombus for each of the four CFD

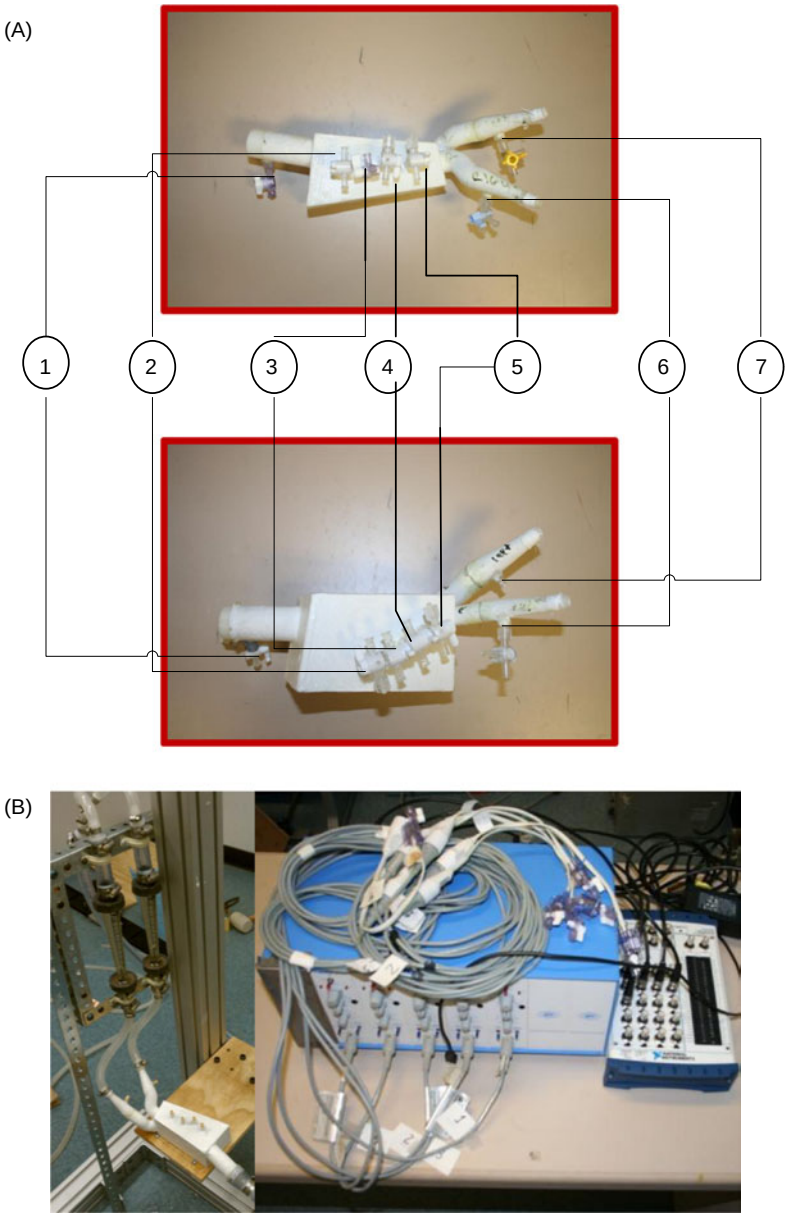

Figure 6. (A) Numbering of the pressure taps for both models [top, with ILT; bottom, without ILT] and (B) details of the flow loop set-up and the pressure measurement equipment.

simulations. The pressure distribution is reasonably homogeneous in the AAA sac and the proper pressure gradient occurs at the inlet of the iliac arteries. In order to distinguish the pressure distribution in these two zones having different characteristics, the sac and iliac inlets, two colour legend ranges have been used for each zone. In Figure 7-top, the legend ranges from 0 to −800 Pa; however, in Figure 7-bottom, it ranges from −800 to −5000 Pa.

The contour plots provided in Figure 7 indicate that at the inlet of the AAA sac, there is an increase of pressure at one side (due to an impingement of a jet flow) as well as a decrease of pressure due to the flow detachment (where the pressure tap is located). Downstream of this pressure tap, the flow is like a jet with a swirling component and the pressure field has a helicoidal shape. The small pressure variations are observed on the spatial locations where flow impingements exist. In addition, the large pressure gradient takes place at the entry region of the iliac arteries.

The Realizable $k-\varepsilon$ model is a turbulent model based on the time-average Navier–Stokes equations. As mentioned above, there are two ways to study a flow with constant flow rate inlet conditions. The first is by using a steady simulation and the second by using a transient

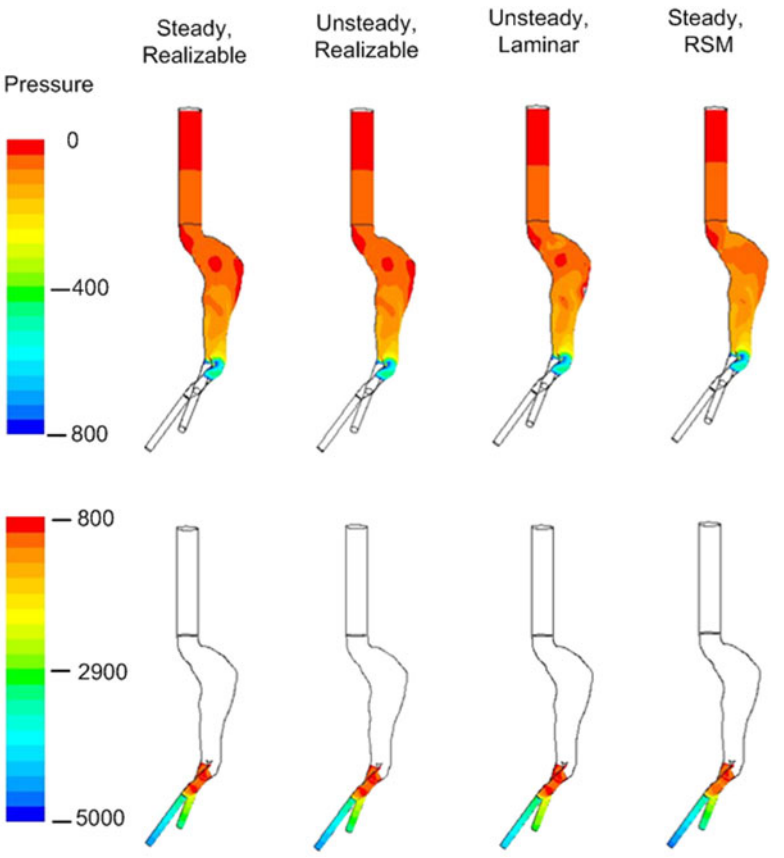

Figure 7. CFD-predicted pressure field in the model with ILT. Computations using four different models: (A) steady $k-\varepsilon$ Realizable, (B) unsteady $k-\varepsilon$ Realizable, (C) unsteady laminar and (D) steady RSM.

simulation but with steady inflow conditions. In general, due to the diverging geometry of the flow domain and jet flow characteristics, flow unsteadiness is likely to appear. In this case, it is expected that the numerical results obtained with a steady and a transient simulations will deviate from each other. Based on our numerical results, no major differences between the steady and transient simulations are observed (see Figure 7), which implies that intrinsic unsteady effects are minor. One important observation inferred from this finding is that the ILT geometry surpasses flow unsteadiness that may have once existed in the sac before ILT formation. The relative differences between experimental (Exp) and computed pressures from CFD are summarised in Table 2.

The *Re* corresponding to peak systolic flow ($Re = 2233$) is close to the theoretical onset of turbulence (in a smooth pipe with a circular cross section). In a complex geometry such as the present one, the onset of turbulence may be associated with a smaller critical *Re*. While acknowledging that the Realizable $k-\varepsilon$ and RSM models are targeted for modelling at high Reynolds numbers, they are able to predict the spatial pressure drop better than the more direct unsteady laminar simulation (see Table 2). The latter modelling option is known to be useful for other cardiovascular applications (Botara et al. 2010). The RSM performed better in predicting the spatial pressure drop for the model with ILT. This is expected because RSM is a second-moment turbulence model that is able to predict the flow more

Table 2. Pressure drop comparison (experimental vs. CFD) for the AAA model with ILT.

Pressure drop (Pa)	Inlet-left iliac	%	Inlet-right iliac	%	Average	%
Experiments (AAA with ILT)	5262.1		4321.8		4792.0	
Steady, Realizable $k-\varepsilon$	4563.5	−13.3	3313.1	−23.3	3938.3	−17.8
Steady, RSM	4683.8	−11.0	3427.8	−20.7	4055.8	−15.4
Unsteady, Realizable $k-\varepsilon$	4560	−13.3	3309	−23.4	3934.5	−17.9
Unsteady, laminar flow	4202.5	−20.1	3020.7	−30.1	3611.6	−24.6

Note: The comparison is expressed as follows: [(CFD − Exp)/Exp] × 100.

accurately than the eddy viscosity models for cases with complex flow as in the present case.

3.1.2 AAA without ILT

Figure 8 presents the predicted pressure field in the AAA model with no ILT. Three CFD simulations with the following mathematical models were performed: first, a steady simulation using the Realizable $k-\varepsilon$ model; second, an unsteady simulation (with constant boundary conditions) also using the Realizable $k-\varepsilon$ model; and third, an unsteady laminar simulation (with constant boundary conditions). For this geometry, the RSM did not converge satisfactorily and is not reported in this manuscript.

As in Section 3.1.1, the pressure is relatively homogeneous in the AAA sac and a large pressure gradient occurs, also at the entry region of the iliac arteries. To properly distinguish the pressure distribution in these two very different zones, sac and iliac inlets, two colour legend ranges have been used for each zone. In Figure 8-top frames, the colour legend ranges from 0 to -300 Pa; however, in Figure 8-bottom frames, it ranges from -300 to -1900 Pa (the pressure at the outlets is set to 0 Pa). As mentioned previously, there is a large difference in total spatial pressure drop between the two models, approximately 1500 Pa for the AAA without ILT and 5000 Pa for the AAA with ILT. This difference can have important physiological effects during AAA growth and peripheral adaptation.

From a physical point of view, a jet coming in the sac is readily detected together with a decreased velocity and a weak vortex appears. The velocity reduction confirms the large reduction in the pressure drop. Flow in the sac region is unstable as it can be also inferred from the small differences between the steady and the unsteady with the Realizable $k-\varepsilon$ model simulation results. The difference between Exp and CFD pressures is summarised in Table 3.

The AAA sac is an enlargement of the aorta that may foster some unsteady flow structure. The unsteady laminar prediction is the best model among the ones presented in Table 3. There is not a large difference between laminar and turbulent predictions. This implies on the one hand that no general conclusion about the flow regime can be drawn and on the other hand that the importance to use or not to use a turbulent model is just a difference within 10%. It is clear that this enlargement may foster the growth of further unsteady flow structures. This may be the reason why the unsteady laminar prediction emerged as the best

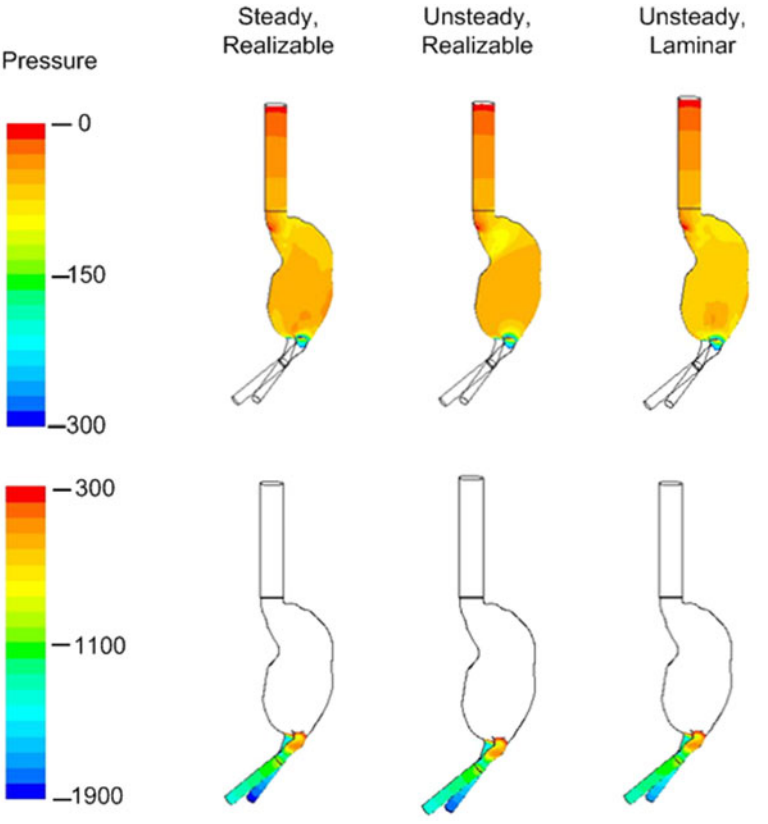

Figure 8. CFD-predicted pressure field in the model without ILT. Computations using three different models: (A) steady $k-\varepsilon$ Realizable, (B) unsteady $k-\varepsilon$ Realizable and (C) unsteady laminar.

Table 3. Pressure drop comparison (experimental vs. CFD) for the AAA model without ILT.

Pressure drop (Pa)	Inlet-left iliac	%	Inlet-right iliac	%	Average	%
Experiments (AAA without ILT)	1341.7		1679.5		1510.6	
Steady, Realizable-$k-\varepsilon$	1381	2.9	1877.3	11.8	1629.2	7.8
Unsteady, Realizable $k-\varepsilon$	1395	4.0	1823	8.5	1609	6.5
Unsteady, laminar flow	1345	0.2	1708.6	1.7	1526.8	1.1

Note: The comparison is expressed as follows: [(CFD − Exp)/Exp] × 100.

model among the alternative ones studied in this manuscript (Table 3).

3.1.3 *Summary of the CFD-experimental comparison*

In general, CFD modelling predicted the pressure fields reasonably well and in good agreement with the qualitative trends. The average difference is 1.1% for the model without ILT and 15.4% for the model with ILT. These differences between the CFD and experimental values are not only due to the fact that there is no perfect turbulence model but also to uncertainties in the inlet boundary conditions. The uncertainty in the application of the CFD flow inlet boundary condition is estimated at 5% (due to the flow meter uncertainty).

3.2 *Local experimental-CFD analysis*

Figure 9 shows the spatial pressure drop between the inlet (location 1) and other locations within each of the aneurysm models (with and without ILT). The error bars in Figure 9 indicate the standard deviation of the four measurements taken at the inlet and the outlets or the standard deviation of the two measurements taken in each of the taps in the aneurysm sac.

Pressure variations along the AAA with and without ILT are qualitatively the same. There is moderate pressure gradient at the inlet of the sac, but in general, the pressure is relatively uniform in the sac for both models. The major pressure gradient in both models occurs between the AAA sac and the common iliac arteries (locations 6 and 7). However, quantitatively, there is a noticeable difference in

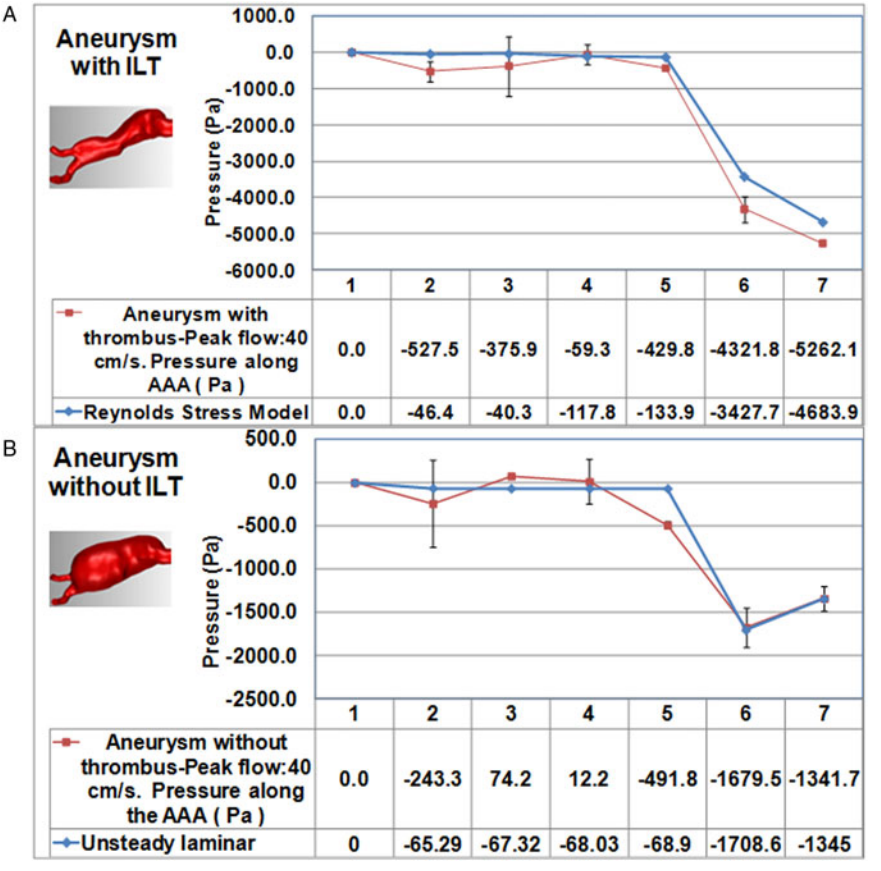

Figure 9. Pressure measurements and CFD predictions along the AAA model with (A) and without ILT (B).

the two aneurysm models. In the model with no ILT, the spatial pressure drop is around 1500 Pa while in the model with ILT, this pressure rises to a value of 5000 Pa (with the flow rate being the same in both models). In the case with ILT, such a spatial pressure drop increase is expected because the smaller the lumen, the higher the flow velocities. This, together with a small decrease in the diameter of the iliac arteries (also due to the thrombus formation) yields a larger hydraulic resistance and as a consequence a larger spatial pressure drop.

Figure 9 clearly shows that the main spatial pressure drop that takes place at the inlet of the iliacs (locations 6 and 7) is very well predicted by CFD for the AAA with ILT and relatively well predicted for the AAA with ILT. CFD predicts a very uniform pressure field in the AAA sac for both with and without ILT. The CFD pressure prediction along the sac in the AAA is within the uncertainty bars of the experimental values. However, for the AAA without ILT, there is a local value (location 5) that is overpredicted by CFD. It seems the CFD model is not able to reproduce some local details of the flow. However, the main pressure drops (locations 6 and 7) are well predicted, and these are the important ones in this analysis.

ILT causes the lumen to reacquire a size similar to that of a healthy abdominal aorta. Moreover, it appears that ILT dampens the flow-induced forces acting on the arterial wall (Bluestein et al. 2009). However, this also leads to an increase in the spatial pressure drop due to both a decrease in the AAA luminal cross-section and a small decrease in the luminal cross-section of the common iliac arteries. Furthermore, as the abdominal aorta is stiff in its diseased state, this increase in spatial pressure drop (due to the presence of ILT) can potentially lead to fatigue rupture (attributable to the pulsatile nature of the blood flow together with subsequent wall weakening caused by the larger pressure gradient at the peak systolic).

3.3 Limitations

In the present work, our major assumption is that the aneurysm formed first and then the accompanying chronic vascular response triggered the thrombus formation. This is a limitation because it is not the normal AAA development. However, it has been found that in 25% of the AAA, there is enlargement without ILT formation (Harter et al. 1983), and therefore, not always the enlargement of the aorta and the formation of ILT develop in parallel. This approach-limitation has already been used to study the flow patterns in Bluestein et al. (2009). Analysing the difference in the pressure field before and after thrombus formation illustrates the changes in mechanical parameters between these two lumped time-points of ILT growth. We believe that this is a first approach necessary to study the effect of thrombus formation on AAA sac pressure and haemodynamics.

At peak systole, the pressure gradient is maximum; during diastole, the pressure gradient is negligible. Therefore, an analysis of steady state flow using boundary conditions based on flow rates at peak systole is a good representation or order of magnitude analysis of the cyclic pressure gradient that takes place continuously in the AAA. However, this is still an approximation of an event that occurs periodically under pulsatile flow conditions and, hence, a limitation of our work.

The estimated pressure fields can provide guidance to clinical catheterisation measurement protocols. AAA rupture occurs when intraluminal pressure reaches a threshold that causes the wall stress to exceed the yield stress of the diseased tissue. Therefore, the assessment of the pressure field is directly related to AAA rupture risk, including the steep changes in its spatial distribution, which is the focus of this work. However, even if the dramatic pressure gradient between the inlet and the iliacs and the large difference for the cases with and without ILT may be patient-dependent; it is believed that it is very important to point out that such cases exist and that those high spatial pressure drops that appear in each cycle may yield a progressive weakening of the wall due to fatigue.

3.4 Final remarks

The present work confirmed that the pressure field is relatively uniform in the AAA sac, excluding the aneurysm neck and aorto-iliac bifurcation. While there is a small pressure gradient at the inlet of the sac (due to jet detachment), the main pressure gradient occurs at the proximal end of the common iliac arteries. Knowledge of the pressure field is important because of its relation to rupture risk assessment. AAA rupture is a mechanical event and variables such as anisotropy of the wall constitutive material, the non-uniform distribution of wall thickness, the absolute pressure and the continuous cyclic pressure gradient at certain locations are hypothesised to relate to rupture risk. In this work, we focused on the spatial pressure drop at peak systole, which is of the same order of magnitude of the maximum cyclic spatial pressure drop and the location of that pressure gradient in the AAA sac.

The presence of ILT in an already formed AAA accounts for a smaller lumen volume, and therefore, it yields larger cyclic spatial pressure drops (5000 Pa) compared to the same AAA sac without ILT (1500 Pa) at the entry region to the common iliac arteries. A large cyclic pressure gradient at the distal end of the aneurysm sac may be a trigger for subsequent wall weakening. Therefore, this work supports the assumption that a likely rupture location is the distal end of the sac. Conversely, the presence of ILT yields flow structures devoid of significant

unsteadiness, similar to those expected for a normal, healthy abdominal aorta. This leads to the observation that unsteady numerical models may not contribute substantially to the CFD fluid flow prediction in AAA models with ILT.

Before ILT formation, there is a jet-like flow pattern coexisting with flow recirculations inside the AAA sac. It is known that this kind of pathology involves low wall shear stresses, which is conducive to platelet deposition at the wall. It is also known that the high shear stresses at the boundaries between the jet and the recirculations are regions where platelet activation is likely (Bluestein et al. 1996). Therefore, these recirculations are zones with high residency times for those activated platelets, a possible explanation for ILT formation. They are also zones prone to have unsteadiness and vortices, which is why unsteady numerical models are preferred for AAA geometries without significant ILT because these models are able to predict the unsteady flow structures.

Finally, CFD simulations implemented with high-performance solvers are able to predict the spatial pressure drop in an AAA model when compared to bench-top experiments within a reasonable relative difference. Although blood flow is mainly laminar through most of the cardiac cycle, at peak systole, the flow reaches the onset of turbulence, notwithstanding a temporary state. Turbulent models, however, may predict constant flow rate conditions modelled at peak systole more reliably.

Acknowledgements

The authors want to acknowledge the help of Samarth Raut for the initial segmentation of the DICOM images and Onur Dur for his help with the pressure transducer calibration. The content is solely the responsibility of the authors and does not necessarily represent the official views of the National Institutes of Health.

Funding

The scholarship was granted by the Spanish Government to R.A. under the 'José Castillejo' program and the Antonio Aranzabal Foundation. This work was supported in part by the National Institutes of Health through award 1R15HL087268-01A2 (to EAF).

References

Antiga L, Ene-Iordache B, Caverni L, Cornalba GP, Remuzzi A. 2002. Geometric reconstruction for computational mesh generation of arterial bifurcations from CT angiography. Comput Med Imaging Graph. 26(4):227–235.

Biasetti J, Gasser TC, Auer M, Hedin U, Labruto F. 2010. Hemodynamics of the normal aorta compared to fusiform and saccular abdominal aortic aneurysms with emphasis on a potential thrombus formation mechanism. Ann Biomed Eng. 38(2):380–390.

Bluestein D, Dumont K, De Beule M, Ricotta J, Impellizzeri P, Verhegghe B, Verdonck P. 2009. Intraluminal thrombus and risk of rupture in patient specific abdominal aortic aneurysm – FSI modelling. Comput Methods Biomech Biomed Eng. 12(1):73–81.

Bluestein D, Niu L, Schoephoerster RT, Dewanjee MK. 1996. Steady flow in an aneurysm model: correlation between fluid dynamics and blood platelet deposition. J Biomech Eng. 118 (3):280–286.

Botara CC, Vasileb T, Sfrangeub S, Clichicic S, Agachia PS, Badeab R, Mircead P, Cristeaa MV. 2010. Validation of CFD simulation results in case of portal vein blood flow. Comput Aided Chem Eng. 28:205–210.

Chen C-Y, Antón R, Hung M-Y, Menon PG, Finol EA, Pekkan K. 2014. Effect of intraluminal thrombus on patient-specific abdominal aortic aneurysm hemodynamics via stereoscopic PIV and CFD modeling. J Biomech Eng. doi: 10.1115/1.4026160.

Di Martino ES, Guadagni G, Fumero A, Ballerini G, Spirito R, Biglioli P, Redaelli A. 2001. Fluid–structure interaction within realistic three-dimensional models of the aneurysmatic aorta as a guidance to assess the risk of rupture of the aneurysm. Med Eng Phys. 23(9):647–655.

Dorfmann A, Wilson C, Edgar ES, Peattie RA. 2010. Evaluating patient-specific abdominal aortic aneurysm wall stress based on flow-induced loading. Biomech Model Mechanobiol. 9:127–139.

Finol EA, Amon CH. 2002. Flow-induced wall shear stress in abdominal aortic aneurysms: Part II – pulsatile flow hemodynamics. Comput Methods Biomech Biomed Eng. 5(4):319–328.

Fluent 12.1. 2010. Fluent user manuals. Canonsburg, PA: Ansys, Inc.

Frauenfelder T, Lotfey M, Boehm T, Wildermuth S. 2006. Computational fluid dynamics: hemodynamic changes in abdominal aortic aneurysm after stent-graft implantation. Cardiovasc Intervent Radiol. 29:613–623.

Gambit 2.4. 2010. Gambit manuals. Canonsburg, PA: Ansys, Inc.

Harter LP, Gross BH, Callen RA, Barth RA. 1983. Ultrasonic evaluation of abdominal aortic thrombus. J Ultrasound Med. 1:315–318.

Launder BE, Reece GJ, Rodi W. 1975. Progress in the development of a Reynolds stress turbulence closure. J Fluid Mech. 68:537–566.

Launder BE, Spalding DB. 1974. The numerical computations of turbulent flows. Comput Methods Appl Mech Eng. 3:269–289.

Newman AB, Arnold AM, Burke GL, O'Leary DH, Manolio TA. 2001. Cardiovascular disease and mortality in older adults with small abdominal aortic aneurysms detected by ultrasonography: the cardiovascular health study. Ann Intern Med. 134(3):182–190.

O'Rourke MJ, McCullough JP. 2010. An investigation of the flow field within patient-specific models of an abdominal aortic aneurysm under steady inflow conditions. Proc Inst Mech Eng H. 224(8):971–988.

Peattie RA, Riehle TJ, Bluth EI. 2004. Pulsatile flow in fusiform models of abdominal aortic aneurysms: flow fields, velocity patterns and flow-induced wall stresses. J Biomech Eng. 126:438–446.

Rodriguez JF, Martufi G, Doblare M, Finol EA. 2009. The effect of material model formulation in the stress analysis of abdominal aortic aneurysms. Ann Biomed Eng. 37(11):2218–2221.

Sakalihasan N, Limet R, Defawe OD. 2005. Abdominal aortic aneurysm. Lancet. 365(9470):1577–1589.

Salsac AV, Sparks SR, Chomaz JM, Lasheras JC. 2006. Evolution of the wall shear stresses during the progressive enlargement of symmetric abdominal aortic aneurysms. J Fluid Mech. 560:19–51.

Scotti CM, Finol EA. 2007. Compliant biomechanics of abdominal aortic aneurysms: a fluid–structure interaction study. Comput Struct. 85(11–14):1097–1113.

Scotti CM, Jimenez J, Muluk SC, Finol EA. 2008. Wall stress and flow dynamics in abdominal aortic aneurysms: finite element analysis vs. fluid–structure interaction. Comput Methods Biomech Biomed Eng. 11(3):301–322.

Scotti CM, Shkolnik AD, Muluk SC, Finol EA. 2005. Fluid–structure interaction in abdominal aortic aneurysms: effects of asymmetry and wall thickness. Biomed Eng Online. 4:1–22.

Shih T-S, Liou WW, Shabbir A, Yang Z, Zhu J. 1995. A new $k-\varepsilon$ eddy viscosity model for high Reynolds number turbulent flows. Comput Fluids. 4(3):227–238.

Shum J, Di Martino ES, Goldhammer A, Goldman D, Acker L, Patel G, Ng JH, Martufi G, Finol EA. 2010. Semi-automatic vessel wall detection and quantification of wall thickness in computed tomography images of human abdominal aortic aneurysms. Med Phys. 37(2):638–648.

Shum J, Martufi G, Di Martino ES, Washington CB, Grisafi J, Muluk SC, Finol EA. 2011. Quantitative assessment of abdominal aortic aneurysm geometry. Ann Biomed Eng. 39 (1):277–286.

Shum J, Xu A, Chatnuntawech I, Finol EA. 2011. A framework for the automatic generation of surface topologies for abdominal aortic aneurysm models. Ann Biomed Eng. 39 (1):249–259.

Swillens A, Lanoye L, De Backer J, Stergiopulos N, Verdonck P, Vermassen F, Segers P. 2008. Effect of an abdominal aortic aneurysm on wave reflection in the aorta. IEEE Trans Biomed Eng. 55(5):1602–1611.

Thompson MM. 2003. Controlling the expansion of abdominal aortic aneurysms. Br J Surg. 90:897–898.

Wolfshtein M. 1969. The velocity and temperature distribution of one-dimensional flow with turbulence augmentation and pressure gradient. Int J Heat Mass Transfer. 12:301–318.